



ZnSnO₃ hollow nanospheres/reduced graphene oxide nanocomposites as high-performance photocatalysts for degradation of metronidazole

Shuying Dong^a, Jingyu Sun^{b,1}, Yukun Li^a, Chongfei Yu^a, Yihui Li^c, Jianhui Sun^{a,*}

^a School of Environment, Henan Normal University, Key Laboratory for Yellow River and Huai River Water Environmental and Pollution Control Ministry of Education, Henan Key Laboratory for Environmental Pollution Control, Xinxiang, Henan 453007, PR China

^b Department of Materials, University of Oxford, Parks Road, Oxford OX1 3PH, United Kingdom

^c School of Chemistry and Chemical Engineering, Henan Normal University, Xinxiang, Henan 453007, PR China

ARTICLE INFO

Article history:

Received 3 April 2013

Received in revised form 7 July 2013

Accepted 15 July 2013

Available online 24 July 2013

Keywords:

ZnSnO₃

Hollow nanosphere

Graphene oxide

Metronidazole

Photocatalytic

ABSTRACT

The fabrication of novel ZnSnO₃ hollow nanospheres/reduced graphene oxide (RGO) hybrid nanocomposite is reported for the first time. The nanocomposites were synthesized *via* a facile route, and were well characterized with the aid of XRD, FTIR, SEM, TEM, BET, UV-vis, and PL techniques. Moreover, the synthesized nanocomposites were used as photocatalysts in the application of the degradation of pharmaceutical wastewater. In this study, ZnSnO₃ hollow nanospheres showed high efficiency in photocatalytic degradation of metronidazole under ultraviolet (UV) light irradiation. More interestingly, the photocatalytic activities of these nanospheres could be enhanced by coupling with RGO, where a large improvement (approx. 30.4% increase compared with pure ZnSnO₃) in photodegradation of metronidazole was observed on the prepared ZnSnO₃/RGO hybrid nanocomposites under visible light irradiation. This improvement might be attributed to the advanced adsorption efficiency of molecules and enhanced visible light absorption within the hybrid nanocomposites by the introduction of RGO. Such study might pave the way toward designing novel photocatalyst systems for efficient degradation of pharmaceutical wastewater.

© 2013 Elsevier B.V. All rights reserved.

1. Introduction

As a common nitroimidazole antibiotic derivative, metronidazole (2-methyl-5-nitroimidazole-1-ethanol) was abused for treating infections caused by a wide range of anaerobic bacteria, bacteroides and protozoa, including trichomoniasis, amoebiasis and gingivitis [1–3]. The maximum concentration of metronidazole at 9400 and 127 ng L⁻¹ have been found in the effluents of hospital and sewage treatment plant, respectively [4,5]. Being as a pharmaceutical substance as well as a potential carcinogen, metronidazole was prone to accumulating in aquatic environments, leading to the pollution of surface water and groundwater [6]. However, the removal efficiency of metronidazole remains to be quite low by employing conventional sewage treatment methodologies [7]. Hence it is imperative to effectively remove metronidazole from the wastewater with the aid of relevant treatment techniques.

Recent development of wastewater treatment technologies has enabled high-efficiency removal of pharmaceutical substances

in the aqueous environment, amongst which the photocatalytic degradation technique has been specifically utilized. The advantage of the photocatalytic degradation technique lies mainly in the fact that it employs low-cost, environment-friendly semiconductor materials (e.g. ZnO) for complete mineralization of complex-structured organics (including pharmaceutical substances) [8,9]. Interest in ZnO for pollution treatment has been stimulated by its great photocatalytic capacity in the degradation of organic pollutants [10,11], and its photocatalytic efficiency can be further improved *via* various approaches such as introducing dopants, in order to suppress the fast-rated recombination of photogenerated electron/hole pairs within the material [12–14]. One of our recent studies has demonstrated that Sn-modified ZnO nanomaterials were characterized with increased sunlight photocatalytic activities (compared to the single-phase ZnO), where Sn⁴⁺ functioned as a good n-type dopant with extensive solid solubility in ZnO and similar value of the atomic radius with Zn²⁺ (Sn⁴⁺: 0.069 nm, Zn²⁺: 0.074 nm) [15].

It is well realized that the photocatalytic performances of photocatalysts strongly depends on the sizes and shapes of employed materials, especially at the nanoscale. Recent studies have shown that hollow-structured ZnO-based nanomaterials could act as promising photocatalysts, owing to their high specific surface area, good permeability, and high interfacial charge-transfer efficiency

* Corresponding author. Tel.: +86 373 3325971; fax: +86 373 3326336.

E-mail address: sunjh@htu.cn (J. Sun).

¹ Current address: Center for Nanochemistry (CNC), College of Chemistry and Molecular Engineering, Peking University, Beijing 100871, PR China.

[16–18]. Wang et al. reported the fabrication of single-crystalline $ZnSn(OH)_6$ hollow cubes *via* a facile self-templating method at room temperature. They also revealed that the photocatalytic performance of $ZnSn(OH)_6$ hollow cubes used for phenol degradation was much higher than that of the solid $ZnSn(OH)_6$ cubes [16]. Yu and colleagues managed to synthesize ZnO hollow nanospheres using $ZnCl_2$ and glucose as starting materials and showed that the obtained hollow nanospheres were of high quality and good stability [18].

Research in the field of graphene (along with graphene-oxide and reduced graphene-oxide) has grown rapidly in the past few years [19]. In photocatalysis, graphene has proven to be an ideal support for forming photocatalytic nanocomposites, owing to its unique electronic properties, large specific surface area, and high optical transparency [20–25]. The graphene-supported nanocomposites possess many novel features in photodegradation of organic pollutants, such as efficient charge transportations and separations, extended light absorption ranges and good adsorption rates of pollutants [23–25]. For example, a recent study performed by Li et al. on using ZnO /graphene-oxide (ZnO/GO) nanocomposites in photodegradation of organic dye showed that GO-supported ZnO facilitated electron collection and transportation, thereby effectively circumventing charge carrier recombination and leading to continuous generation of reactive oxygen species for the degradation of dye [23]. However, there have few reports on decorating graphene nanosheets with well-organized hollow inorganic nanostructures, the combination of which is expected to possess superior performances as photocatalysts for the photodegradation of pollutants.

Herein, we report facile synthesis of $ZnSnO_3$ hollow nanospheres/reduced graphene oxide (RGO) hybrid ($ZnSnO_3/RGO$) nanocomposites, with first-time usage of these novel nanocomposites for the application of pollutant degradation. In this work, Both $ZnSnO_3$ hollow nanospheres and $ZnSnO_3/RGO$ nanocomposites have been targetedly fabricated, well characterized, and carefully evaluated in the investigations of degradation of metronidazole-contained wastewater under UV or visible light irradiation. In particular, the $ZnSnO_3/RGO$ nanocomposites have displayed enhanced visible-light-driven photocatalytic performance.

2. Experimental

2.1. Synthesis of $ZnSnO_3$ hollow nanospheres/RGO ($ZnSnO_3/RGO$) nanocomposites

All the chemicals were analytical grade reagents and used as received without further purification. Deionized water was used throughout this study.

2.1.1. Synthesis of graphene oxide (GO)

GO was synthesized from natural graphite powder according to the recipe described by a modified Hummers' method [26]. In detail, 1 g graphite was slowly added into 23 mL concentrated H_2SO_4 equipped within an ice-water bath. After 10 min stirring, 3 g $KMnO_4$ was added into the mixture, followed by 1 h reaction. The obtained dark green reaction mixture was then shifted to 30 °C with continuous stirring for 1 h. As the next step, 46 mL deionized water was added drop by drop, where the heating temperature was maintained at 96 °C for 30 min. Finally, 10 mL H_2O_2 and 140 mL deionized water were added to cease the reaction. The mixture was then centrifuged at 4000 rpm for 10 min, followed by washing through alternatively using 5% HCl aqueous solution/ethanol for several times. The collected precipitate was dried at 60 °C for 12 h without any further purification.

2.1.2. Synthesis of $ZnSnO_3$ hollow nanospheres

The template (carbon nanospheres) was prepared according to a reported procedure [27]. In a typical $ZnSnO_3$ hollow nanosphere synthesis, 1 g $SnCl_2 \cdot 2H_2O$ was dissolved in 50 mL HCl solution (6 M) with gentle heating, followed by adding 15 g $Zn(CH_3COO)_2 \cdot 2H_2O$ into the solution. 0.2 g prepared carbon spheres were added and ultrasonicated for 1 h, followed by continuous stirring for 24 h. The dark precursor was then collected by filtration, washed by deionized water and ethanol, and dried at 100 °C in an oven overnight. Final products (white-colored) could be obtained after calcinating the precursor at 600 °C for 2 h in a muffle furnace.

2.1.3. Synthesis of $ZnSnO_3/RGO$ nanocomposites

0.2 g $ZnSnO_3$ hollow spheres were dispersed in 40 mL 1 mg L⁻¹ GO solution with 1 h sonication and then stirred for 12 h. After adding 0.2 mL ammonia and 0.1 mL hydrazine hydrate, the suspension was placed into a teflon-lined stainless steel autoclave and maintained at 180 °C for 10 h. When it was naturally cooled to room temperature, the composites were processed by filtration, rinsed with water and ethanol for several times, and then dried at 100 °C overnight. For comparison, RGO was fabricated in the absence of $ZnSnO_3$ hollow nanospheres.

2.2. Characterizations

The crystal structure of the prepared GO, RGO, $ZnSnO_3$ hollow nanospheres, and $ZnSnO_3/RGO$ nanocomposites were analyzed by X-ray diffraction (XRD). The patterns were recorded in the 2 θ range of 10–70° with a scan rate of 0.02°/0.4 s using a Bruker-D8-AXS diffractometer system equipped with a Cu K α radiation ($\lambda = 0.15406 \text{ \AA}$) (Bruker Co., Germany). Fourier transform infrared (FT-IR) spectra were recorded using a FTIR Analyzer (Perkin-Elmer, Spectrum 400), and the KBr was served as a reference sample. The morphologies of obtained products were analyzed by using a JSM-6390LV scanning electron microscopy (SEM) and a JEM-2100 high-resolution transmission electron microscopy (HRTEM). The measurements of low-temperature N_2 adsorption were carried out by using a Micromeritics ASAP 2020 apparatus at –196 °C, all the samples were degassed at 100 °C for 6 h prior to the measurement. The photoluminescence (PL) spectra of photocatalysts were recorded using a Fluorescence Spectrophotometer (FP-6500, Japan) equipped with a Xenon lamp at an excitation wavelength of 320 nm. The ultraviolet-visible (UV-vis) spectra of photocatalysts were measured by a UV-Vis spectrophotometer (Lambda 17, Perkin-Elmer) at the wavelength range of 200–900 nm. Prior to UV-vis analysis, the samples were ultrasonically dispersed in deionized water at room temperature.

2.3. Evaluation of photocatalytic activity

The photocatalytic activities of the prepared $ZnSnO_3$ hollow nanospheres and $ZnSnO_3/RGO$ nanocomposites were evaluated through the degradation of metronidazole-contained wastewater. All experiments were carried out in a quartz reactor consisting of a 250 mL glass reaction bulb and a quartz condenser. A 300 W high-pressure mercury lamp and 500 W U-shaped xenon lamp were used as the UV and visible light source (Yaming Company, Shanghai), respectively.

Prior to each test, the lamp was turned on and warmed up for about 10 min in order to establish a constant light output. Batch tests were performed as the following: 0.2 g $ZnSnO_3$ hollow nanospheres or $ZnSnO_3/RGO$ nanocomposites were added into 200 mL metronidazole solution with a concentration of 5 mg L⁻¹. Before illumination, the mixture was magnetically stirred for 40 min in dark to allow the establishment of physical adsorption equilibrium of metronidazole on catalyst particles. Then the

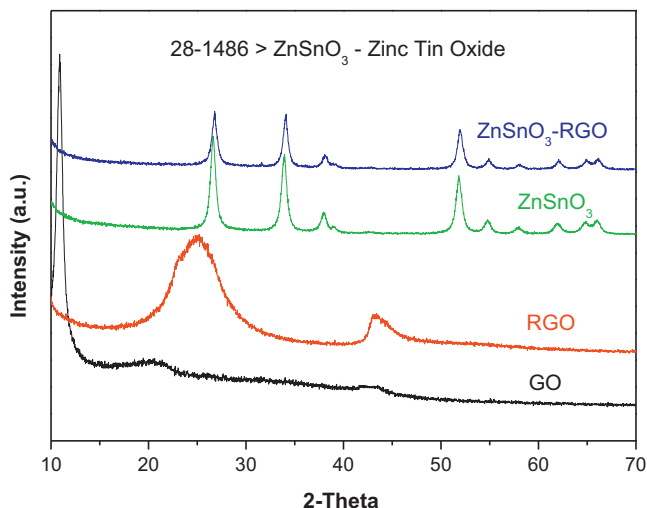


Fig. 1. XRD patterns of GO, RGO, ZnSnO₃ hollow nanosphere and ZnSnO₃/RGO nanocomposites.

solution was exposed to UV or visible light irradiation under magnetic stirring at 500 rpm, which marked the beginning of the photocatalytic degradation tests. An air diffuser was placed at the bottom of the reactor to uniformly disperse air into the solution with a flow rate of 0.2 m³ h⁻¹. 5 mL of the suspension was sampled at each 10 or 30 min intervals, which was immediately centrifuged to remove particles for further analysis.

The concentration of metronidazole was determined by measuring the absorption intensity at its maximum absorbance wavelength of $\lambda = 319$ nm using a UV-Vis spectrophotometer (UV-1700, SHIMADU) with a 1 cm path length spectrometric quartz cell, and was calculated from the calibration curve. The degradation efficiency of the metronidazole-contained wastewater was determined according to the following equation:

$$\text{degradation efficiency (\%)} = \frac{C_0 - C_t}{C_0} \times 100\% \quad (1)$$

where C_0 was the concentration of metronidazole after 40 min adsorption and C_t was the concentration of metronidazole at certain reaction time t (min).

3. Results and discussion

3.1. XRD, FTIR, SEM, TEM, BET, UV-vis, and PL of the synthesized nanocomposites

XRD was employed to characterize the crystal phases of GO, RGO, ZnSnO₃ hollow nanospheres, and ZnSnO₃/RGO nanocomposites, the patterns of which are shown in Fig. 1. The sharp peak at around $2\theta = 10.8^\circ$ (black curve), which corresponds to the (001) reflection of GO [28], almost disappears in the pattern of RGO (red curve). Moreover, the RGO nanosheets exhibit a broad (002) diffraction peak at around $2\theta = 26^\circ$ and a (100) diffraction peak at around $2\theta = 44^\circ$ [29]. The observed peaks of the synthesized ZnSnO₃ hollow nanospheres (green curve) are in good agreement with the standard XRD pattern of ZnSnO₃ (International Center for Diffraction Data, JCPDS 28-1486), which confirms the crystalline nature of obtained samples. The blue curve displays the XRD pattern of the synthesized ZnSnO₃/RGO nanocomposites, where no apparent change in peak shapes and positions are observed in comparison with that of the ZnSnO₃ hollow nanospheres, indicating that the introduction of RGO has no effect upon the crystal orientations of ZnSnO₃. However, it is worth-noting that no typical diffraction peaks of GO or RGO are observed within the blue

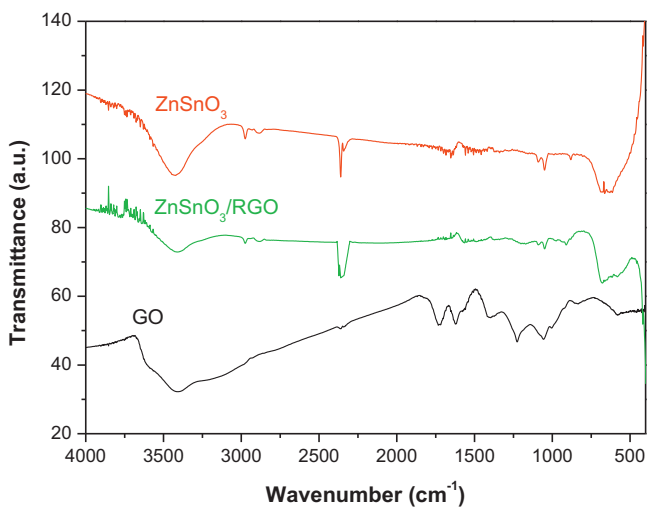


Fig. 2. FTIR spectra of GO, ZnSnO₃ hollow nanosphere and ZnSnO₃/RGO nanocomposites.

curve, the reason of which may be due to the small amount and relatively low diffraction intensity of RGO in the composite [29].

FTIR spectra of GO, ZnSnO₃ hollow nanospheres, and ZnSnO₃/RGO nanocomposites are shown in Fig. 2. The FTIR spectrum of GO (black curve) displays several characteristic bands at 1065, 1219, 1404, 1625, and 1724 cm⁻¹, which correspond to the C—O—C stretching vibrations, the C—OH stretching peak, the O—H deformation of the C—OH groups, the C=C stretching mode and the C=O stretching vibrations of the —COOH group, respectively, indicating the presence of the oxygen-containing functional groups on the surface of GO. The broad band at 3412 cm⁻¹ (black curve) are assigned to O—H stretching vibrations of adsorbed water molecules on GO [30]. Compared to the spectrum of GO, the bands featuring oxygen-containing functional groups almost vanish in the spectrum (green curve) of the ZnSnO₃/RGO nanocomposites, confirming the successful and effective reduction of GO nanosheets. Moreover, the bands at 728, 2368, and 3468 cm⁻¹ for both the samples of ZnSnO₃ hollow nanospheres and ZnSnO₃/RGO nanocomposites are ascribed to the stretching modes of Zn—O and Sn—O [31].

The representative SEM images of the prepared ZnSnO₃ hollow nanospheres and ZnSnO₃/RGO nanocomposites are shown in Fig. 3. Fig. 3a and b presents the top-view SEM observations of the ZnSnO₃ hollow nanospheres. It can be seen from the images that the obtained products are of uniform size distributions. The nanomaterial possesses a hollow sphere structure, as one is able to randomly observe the shell-opened spheres (marked by red circles in Fig. 3b and d). Fig. 3c and d displays the top-view SEM observation of the ZnSnO₃/RGO nanocomposites, although stratiform RGO nanosheets are hardly observed due to the high and uniform coverages of ZnSnO₃ hollow nanospheres on them.

Fig. 4 displays the TEM characterization of the prepared RGO (Fig. 4a and b), ZnSnO₃ hollow nanospheres (Fig. 4c and d), and ZnSnO₃/RGO nanocomposites (Fig. 4e and f), where detailed morphological information of synthesized materials can be obtained. Fig. 4a displays a general view of the produced RGO, with a higher magnified image shown in Fig. 4b. It can be seen from these images that RGO flakes stack with each other and exhibit layered nanostructures. The TEM micrograph in Fig. 4c confirms the formation of hollow nanospheres, where the distinguished contrasts can be found between the outer shells and the inner hollow cores. Also, the hollow nanospheres are of uniform size distributions, with a mean diameter at approx. 260 nm and a mean shell thickness at approx. 7 nm. More close view of the hollow nanospheres is

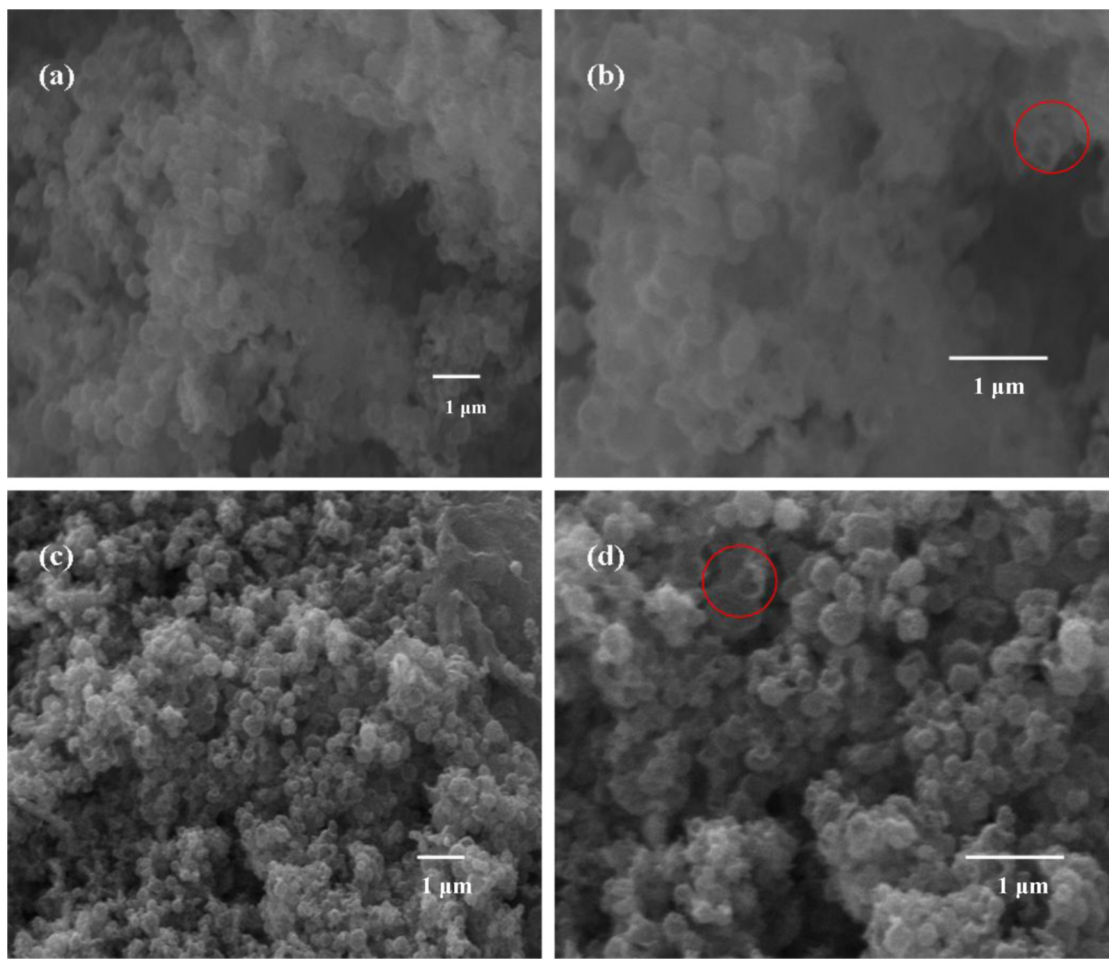


Fig. 3. The SEM images of the prepared ZnSnO_3 hollow nanosphere (a and b) and $\text{ZnSnO}_3/\text{RGO}$ nanocomposites (c and d).

shown in Fig. 4d, revealing that the shells of the nanospheres are not smooth and consist of crystallized nanoparticles with a mean particle size of 6–8 nm, which might contribute to the promising catalytic abilities of these nanospheres. Another feature of the shell is in regards to its high porosity with a mean pore size of 2–4 nm, which makes the hollow sphere a good candidate to accommodate guest species (such as molecules) [32]. The low-magnified TEM observation in Fig. 4e shows the typical wrinkles of RGO nanosheets and uniform coatings of ZnSnO_3 hollow nanospheres, confirming the formation of $\text{ZnSnO}_3/\text{RGO}$ nanocomposites. Higher magnified image in Fig. 4f shows that the nanospheres remain crystallized after contacting with RGO. Both of these images reveal that numerous ZnSnO_3 hollow nanospheres strongly bound to RGO sheets, which are not detached during TEM sample preparation (sonication), this is probably due to the fact that the functional groups on RGO provided active sites for anchoring guest nanomaterials [33].

The surface area of photocatalysts, depended upon the porosity and geometrical shape of the materials, plays an important role in the photocatalytic activity [34]. Table 1 depicts the comparison of the BET surface area, pore volume and pore diameter of both the ZnSnO_3 hollow nanospheres and $\text{ZnSnO}_3/\text{RGO}$ nanocomposites. Information can be extracted from the table that the ZnSnO_3 hollow nanospheres shows a larger specific BET surface area at about $10.2169 \text{ m}^2 \text{ g}^{-1}$, which is higher than that of our previously reported ZnSnO_3 nanoparticles [15]. Notably, that after composited RGO, the specific BET surface area of the $\text{ZnSnO}_3/\text{RGO}$ nanocomposite is even higher than that of the hollow nanosphere by a factor of 5.8. This might partially attributed to the fact that RGO with 2D arrangements possesses large theoretical specific surface area.

To further obtain the pore size distributions of the synthesized nanostructures, nitrogen adsorption-desorption measurements were performed. Fig. 5a shows the nitrogen adsorption-desorption isotherms of the ZnSnO_3 hollow nanosphere and $\text{ZnSnO}_3/\text{RGO}$ nanocomposite samples. Both obtained curves are of type IV (Brunauer Deming Deming Teller (BDDT) classification) isotherms with a H3 typical hysteresis loop, indicating that the pore size distributions of the ZnSnO_3 hollow nanosphere and $\text{ZnSnO}_3/\text{RGO}$ nanocomposite samples are bimodal types locating in the mesoporous region. However, the curve of the $\text{ZnSnO}_3/\text{RGO}$ nanocomposites positions higher on the graph, indicating a correspondingly larger adsorbance, which is consistent with the results that the nanocomposites have a larger BET surface area. Furthermore, the enhanced adsorption behavior in the relatively high pressure (P/P_0) range observed for both samples is a good indication of the presence of large mesopores and macropores within the samples. Fig. 5b shows the corresponding pore size distribution curves

Table 1

Comparison of nitrogen adsorption characteristics of the samples ZnSnO_3 and $\text{ZnSnO}_3/\text{RGO}$.

Sample	BET surface areas ^a ($\text{m}^2 \text{ g}^{-1}$)	Pore volume ^b ($\text{cm}^3 \text{ g}^{-1}$)	Pore diameter ^c (nm)
ZnSnO_3	10.2169	0.055351	200
$\text{ZnSnO}_3/\text{RGO}$	58.1951	0.256712	165

^a BET surface area calculated from the linear part of the BET plot ($p/p_0 = 0.18–0.30$).

^b Total pore volume, taken from the volume of N_2 adsorbed at $p/p_0 = 0.989$.

^c Average pore diameter, estimated using the desorption branch of the isotherm and the Barrett–Joyner–Halenda (BJH) formula.

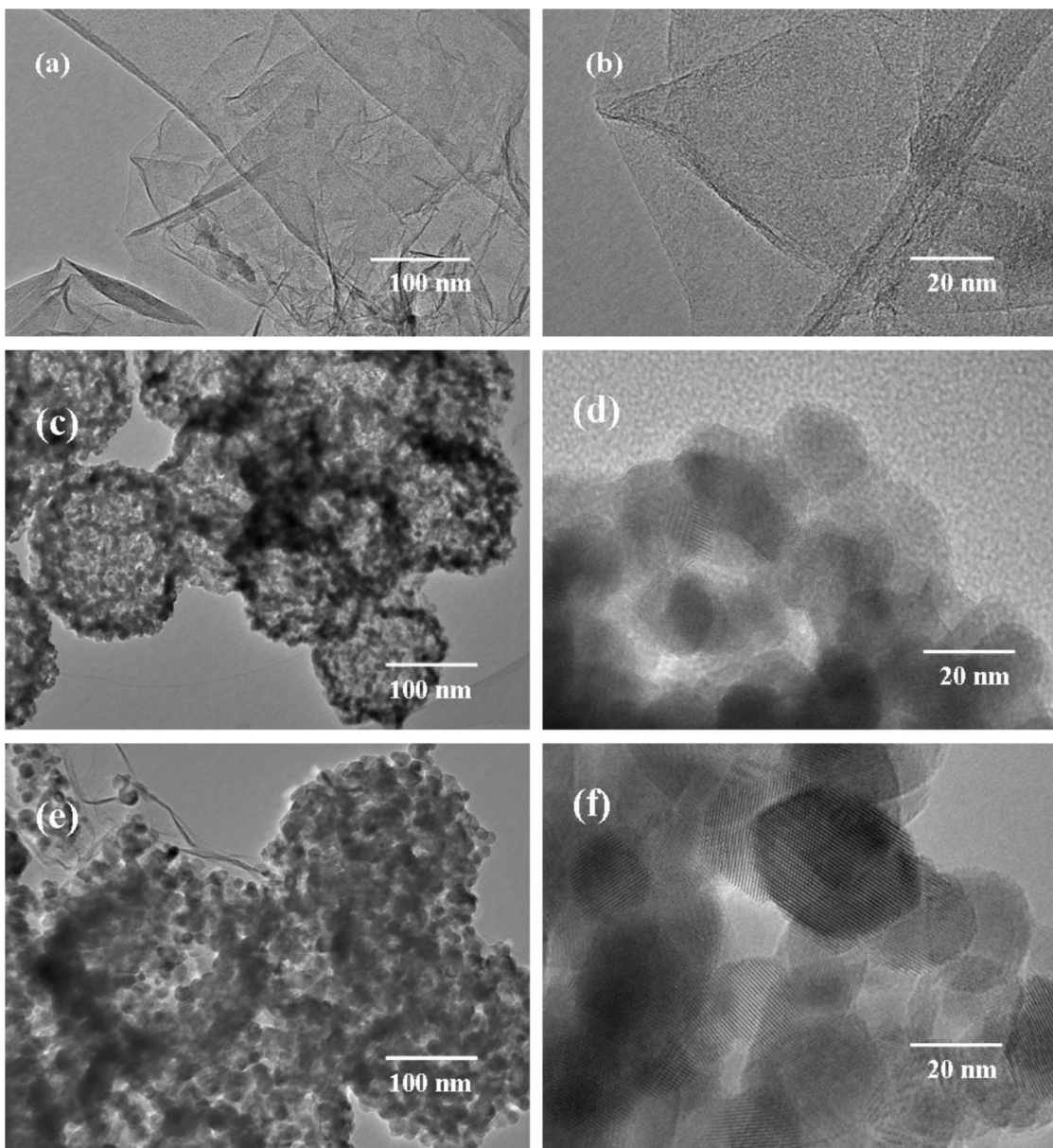


Fig. 4. The HRTEM images of the prepared RGO (a and b), ZnSnO_3 hollow nanosphere (c and d), and ZnSnO_3 /RGO nanocomposites (e and f).

calculated from the adsorption branch of nitrogen isotherm by the BJH method using the Halsey equation [35], where the ZnSnO_3 hollow nanospheres and ZnSnO_3 /RGO nanocomposites are measured with the average pore diameters of 200 and 165 nm, respectively.

The capacity of UV-vis light absorption is an important factor for evaluating optical properties of photocatalysts [36]. UV-vis absorption spectra of the RGO, ZnSnO_3 hollow nanospheres, and ZnSnO_3 /RGO nanocomposites are shown in Fig. 6. It can be seen that the spectrum of RGO displays an absorption peak at around 270 nm (black curve), which is regarded as the trademark for RGO [37]. The spectrum of pure ZnSnO_3 hollow nanospheres displays a broad absorption band edge between 240–300 nm (red curve), which is consistent with previously published results [38]. However, the spectrum of the ZnSnO_3 /RGO nanocomposites red shifts by adding RGO (green curve) and is characterized with enlarged light absorption scope and intensity. This phenomenon of the red shift could be attributed to the increase of planarity due to the connection of RGO with the ZnSnO_3 chains via hydrogen bonding, thus resulting in a more conjugated system [37]. The good

performance in the UV-vis light absorption by the prepared ZnSnO_3 /RGO nanocomposite can lead to its use in visible-light photocatalysis.

Fig. 7 shows the PL spectra of the prepared RGO, ZnSnO_3 hollow nanospheres, and ZnSnO_3 /RGO nanocomposites. The PL spectrum of the ZnSnO_3 hollow nanospheres (black curve) displays a near-band-edge excitonic emission ranging between 360 and 480 nm without a defect-related green band, which could be assigned to blue-violet region. It has been reported that the emission corresponds to the bulk band gap of ZnO originating from the recombination of electrons in single occupied oxygen vacancies. However, the spectrum of the ZnSnO_3 /RGO nanocomposites (red curve) is apparently different from that of the ZnSnO_3 hollow nanospheres, but similar to that of the RGO (green curve), showing a completely quenched manner where there is almost no luminescence occurred. The reason of this might be due to an efficient charge separation process achieved by direct electron transfer from the ZnSnO_3 hollow nanosphere to the RGO via the chemical bonding of $\text{Sn}-\text{Zn}-\text{O}-\text{C}$. These results confirm the RGO can enhance

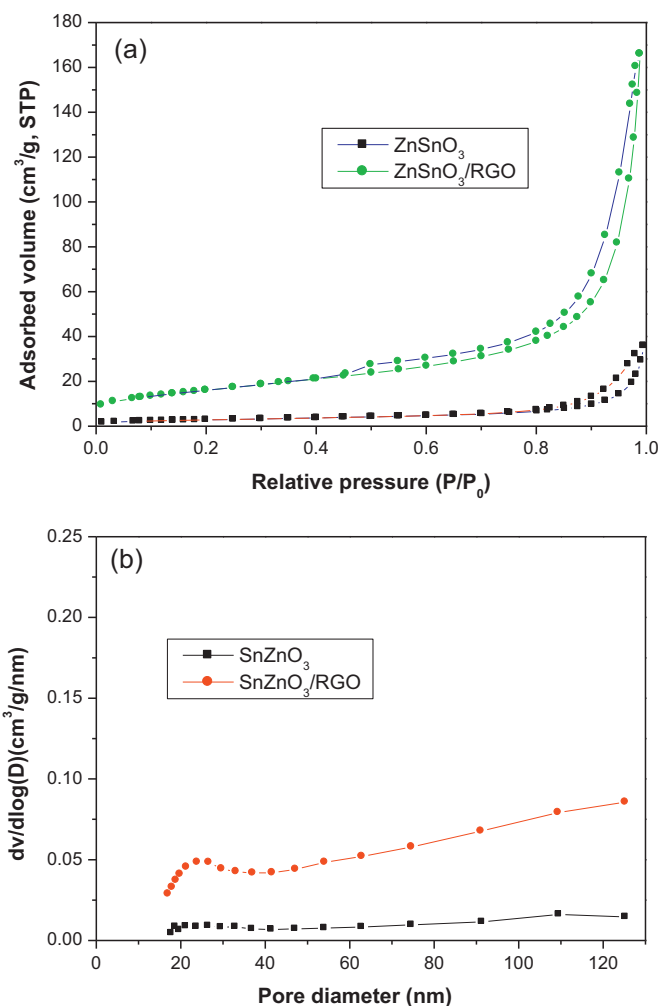


Fig. 5. Nitrogen adsorption desorption isotherms (a) and the corresponding pore size distribution curves (b) of ZnSnO₃ and ZnSnO₃/RGO nanocomposites.

the photo-induced charge transfer within ZnSnO₃/RGO photocatalysts. Previous research has indicated that RGO could act as the electron transfer channel in RGO-supported semiconductor composites, where it helps maintain a lower rate of recombination of electrons and holes, leading to maximized charge separations

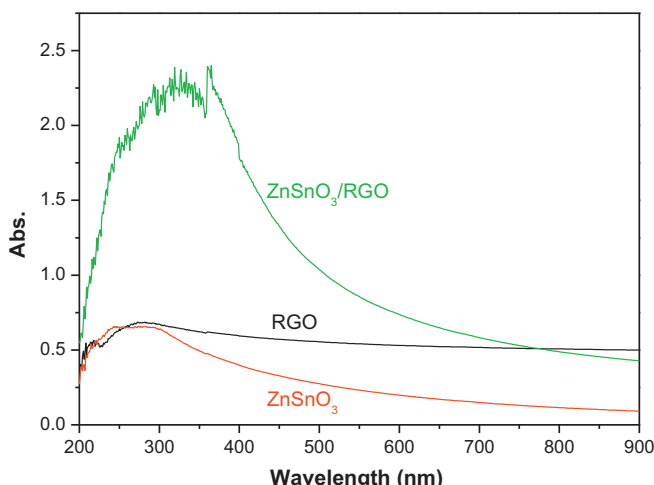


Fig. 6. The UV-vis absorption spectra of the RGO, pure ZnSnO₃ hollow nanosphere and ZnSnO₃/RGO nanocomposites.

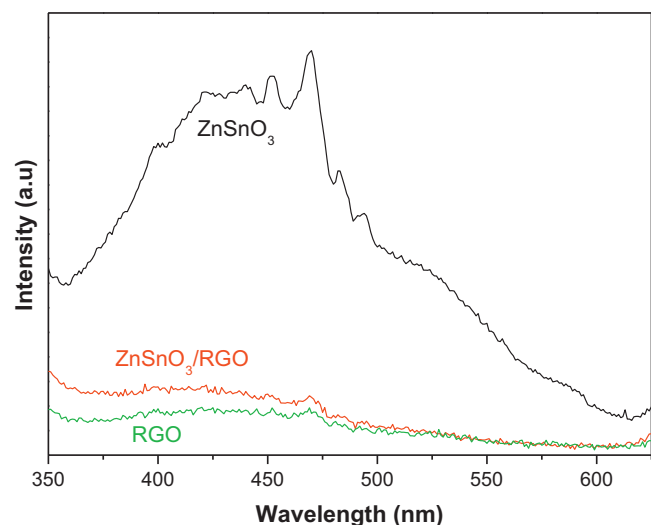


Fig. 7. The PL spectra of the prepared RGO, pure ZnSnO₃ hollow nanosphere and ZnSnO₃/RGO nanocomposites.

thus enhanced material properties [39]. Our results are consistent with the research results stated above, indicating that the prepared ZnSnO₃/RGO nanocomposites might possess great photocatalytic capacities.

3.2. Photocatalytic performances

The applications of the prepared ZnSnO₃ hollow nanospheres and ZnSnO₃/RGO nanocomposites in pharmaceutical wastewater treatment were evaluated by the degradation of metronidazole. The adsorption efficiencies of metronidazole of ZnSnO₃ hollow nanospheres and ZnSnO₃/RGO nanocomposites have been measured to be of 15.4% and 24.2%, respectively (40 min duration). The RGO-supported nanocomposite possessing greater adsorption efficiency is due to the fact that it has bigger BET surface areas and might provide more adsorptive sites, which would accommodate more metronidazole molecules. For the investigations on photocatalytic performances of prepared nanostructures, firstly the photocatalytic degradation of metronidazole using the ZnSnO₃ hollow nanospheres as catalysts are conducted under UV irradiation, the results of which are shown in Fig. 8a. It can be seen that in the presence of the ZnSnO₃ hollow nanospheres, the degradation efficiency of metronidazole increases dramatically, where the degradation process terminates right after 20 min irradiation; whilst in the blank test (absence of the ZnSnO₃ hollow nanospheres), the degradation rate of metronidazole is only about 39.7% even applying 60 min UV irradiation. The results indicate that the prepared ZnSnO₃ hollow nanospheres possess good photocatalytic activity under UV irradiation. The other part of the investigations on photocatalytic performances of prepared nanostructures were concerned with visible light degradation experiments using prepared samples, namely, ZnSnO₃ hollow nanospheres, ZnSnO₃/RGO nanocomposites, pure RGO, and ZnSnO₃-RGO physical mixtures, where the values of surface areas of the last three samples were controlled to be the same, aiming to eliminate potential reason of photocatalytic activity associated with just the surface area increase of RGO. It is noted from the Fig. 8b that, under visible light irradiation (duration: 180 min), the degradation efficiencies of metronidazole with the involvements of the ZnSnO₃ hollow nanospheres and ZnSnO₃/RGO nanocomposites reach at 42.1% (red curve) and 72.5% (green curve), respectively, whilst the pure RGO samples and ZnSnO₃-RGO physical mixtures display extremely poor degradation performances, as shown by the

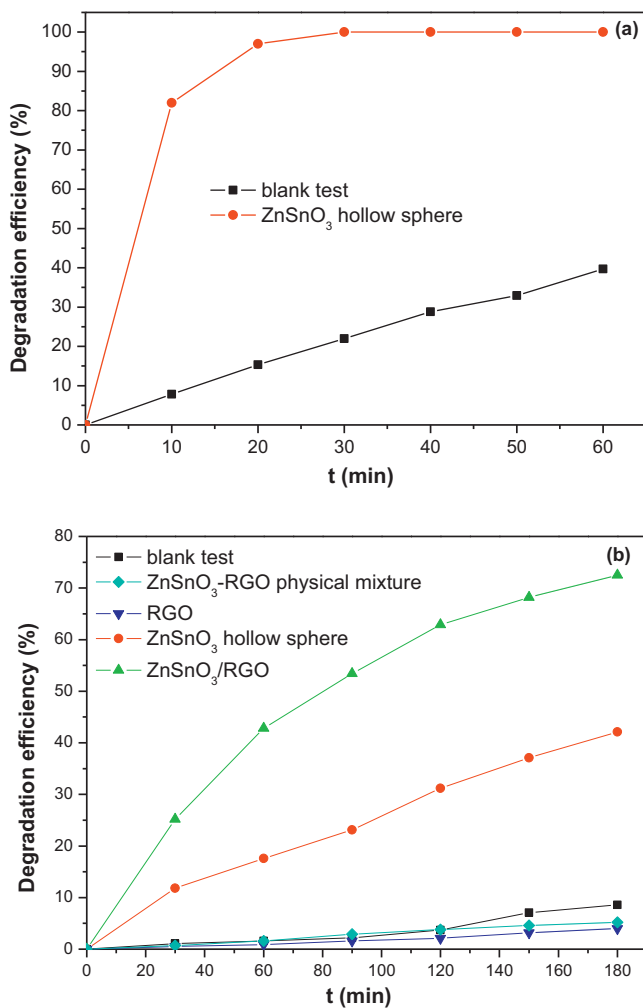


Fig. 8. The degradation efficiencies of the metronidazole wastewater by ZnSnO_3 hollow nanosphere and $\text{ZnSnO}_3/\text{RGO}$ nanocomposites photocatalysts under UV (a) and visible light (b) irradiation.

blue and cyan curve, respectively. The results demonstrate that the mere increase of surface area of RGO during the synthesis of $\text{ZnSnO}_3/\text{RGO}$ nanocomposites might not be one of the potential reasons accounting for the improvement of their photocatalytic activity; the results also indicate that the interaction between the ZnSnO_3 and RGO (rather than their simple mixing) within the nanocomposites is crucial for the photocatalytic performance. Therefore, we speculate that the superior visible-light-driven photocatalytic activity might be attributed to the advanced adsorption efficiency of molecules, enhanced visible light absorption, and unique electronic structures [40–42] of the hybrid nanomaterials with the presence of RGO. Further investigation aims to unravel the ultimate mechanism of photocatalytic degradation involving such inorganic novel architectures (e.g. ZnSnO_3 hollow spheres) and conjugated π -bonding systems (e.g. RGO).

4. Conclusions

In this study, novel ZnSnO_3 hollow nanospheres/reduced graphene oxide hybrid nanocomposites were fabricated for the first time, which were well characterized with the aid of various techniques. The synthesized nanocomposite was used as photocatalyst in the application of the degradation of pharmaceutical wastewater, where it exhibited excellent photocatalytic activity in degradation of metronidazole-contained aqueous solutions under

visible-light irradiation. Future work will be not only focused on the synthesis of other RGO-supported nanocomposites with uniform sizes, unique morphologies, high qualities, and advanced photocatalytic properties, but also the usage of these novel nanocomposites in various application sectors in catalysis. This study might pave the way toward designing novel photocatalyst systems for efficient degradation of pharmaceutical wastewater.

Acknowledgements

The authors are grateful for the financial support from the Basic Scientific and Technological Frontier Project of Henan Province, PR China (Grant Nos. 132330410138, 112300410157, and 122300410293), the Key Science and Technology Program of Henan Province, PR China (Grant No. 132102210129). The authors also would like to thank the Innovation Scientists and Technicians Troop Construction Projects of Henan Province, and the Plan For Scientific Innovation Talent of Henan Province (Grant No. 134200510014).

References

- [1] J.C. Xiao, L.F. Xie, L. Zhao, S.L. Fang, Z.R. Lun, *Parasitology Research* 102 (2008) 613–619.
- [2] G.Z. He, Y.X. Chen, W.Y. Tian, Y. Feng, A.N. Wang, Y. Wei, Q.S. He, C.W. An, *Asian Journal of Animal and Veterinary Advances* 6 (2011) 1026–1030.
- [3] Z.Q. Fang, X.Q. Qiu, J.H. Chen, X.H. Qiu, *Applied Catalysis B: Environmental* 100 (2010) 221–228.
- [4] M.J. Gomez, O. Malato, I. Ferrer, A. Aguera, A.R. Fernandez-Alba, *Journal of Environmental Monitoring* 9 (2007) 718–729.
- [5] R. Rosal, A. Rodriguez, J.A. Perdigon-Melon, A. Petre, E. Garcia-Calvo, M.J. Gomez, A. Aguera, A.R. Fernandez-Alba, *Water Research* 44 (2010) 578–588.
- [6] E. Daeseleire, H. Ruyck, R. Van Renterghem, *Analyst* 125 (2000) 1533–1535.
- [7] K. Yu, B. Li, T. Zhang, *Analytica Chimica Acta* 738 (2012) 59–68.
- [8] J. An, Q.X. Zhou, *Journal of Environmental Sciences-China* 24 (2012) 827–833.
- [9] V. Kitisou, N. Filippidis, D. Mantzavinos, I. Poulios, *Applied Catalysis B: Environmental* 86 (2009) 27–35.
- [10] S. Rehman, R. Ullah, A.M. Butt, N.D. Gohar, *Journal of Hazardous Materials* 170 (2009) 560–569.
- [11] M. Muruganandham, J.J. Wu, *Applied Catalysis B: Environmental* 80 (2008) 32–41.
- [12] D. Li, H. Haneda, *Chemosphere* 54 (2004) 1099–1110.
- [13] H.B. Fu, T.G. Xu, S.B. Zhu, Y.F. Zhu, *Environmental Science and Technology* 42 (2008) 8064–8069.
- [14] K. Yang, B.S. Xing, *Environmental Science and Technology* 43 (2009) 1845–1851.
- [15] J.H. Sun, S.Y. Dong, J.L. Feng, X.J. Yin, X.C. Zhao, *Journal of Molecular Catalysis A: Chemical* 335 (2011) 145–150.
- [16] L.L. Wang, K.B. Tang, Z.P. Liu, D.K. Wang, J. Sheng, W. Cheng, *Journal of Materials Chemistry* 21 (2011) 4352–4357.
- [17] H.B. Zeng, W.P. Cai, P.S. Liu, X.X. Xu, H.J. Zhou, C. Klingshirn, H. Kalt, *ACS Nano* 2 (2008) 1661–1670.
- [18] J.G. Yu, X.X. Yu, *Environmental Science and Technology* 42 (2008) 4902–4907.
- [19] O.C. Compton, S.T. Nguyen, *Small* 6 (2010) 711–723.
- [20] Y. Yokomizo, S. Krishnamurthy, P.V. Kamat, *Catalysis Today* 199 (2013) 36–41.
- [21] P. Madhusudan, J.G. Yu, W.G. Wang, B. Cheng, G. Liu, *Dalton Transactions* 41 (2012) 14345–14353.
- [22] Y.L. Min, K. Zhang, Y.C. Chen, Y.G. Zhang, *Separation and Purification Technology* 86 (2012) 98–105.
- [23] B.X. Li, T.X. Liu, Y.F. Wang, Z.F. Wang, *Journal of Colloid and Interface Science* 377 (2012) 114–121.
- [24] Q.P. Luo, X.Y. Yu, B.X. Lei, H.Y. Chen, D.B. Kuang, C.Y. Su, *Journal of Physical Chemistry C* 116 (2012) 8111–8117.
- [25] X.L. Yu, G.J. Zhang, H.B. Cao, X.Q. An, Y. Wang, Z.J. Shu, X.L. An, F. Hua, *New Journal of Chemistry* 36 (2012) 2593–2598.
- [26] W.S. Hummers, R.E. Offerman, *Journal of the American Chemical Society* 80 (1958) 1339.
- [27] X.M. Sun, Y.D. Li, *Angewandte Chemie International Edition* 116 (2004) 607–611.
- [28] J.S. Chen, Z.Y. Wang, X.C. Dong, P. Chen, X.W. Lou, *Nanoscale* 3 (2011) 2158–2161.
- [29] T. Lv, L.K. Pan, X.J. Liu, T. Lu, G. Zhu, Z. Sun, *Journal of Alloys and Compounds* 509 (2011) 10086–10091.
- [30] H.T. Hu, X.B. Wang, F.M. Liu, J.C. Wang, C.H. Xu, *Synthetic Metals* 161 (2011) 404–410.
- [31] S.J. Ahn, T.G. Kwon, S.Y. Lee, *Journal of Colloid and Interface Science* 362 (2011) 292–299.
- [32] Y.J. Hu, P. Wu, H. Zhang, C.X. Cai, *Electrochimica Acta* 85 (2012) 314–321.

- [33] Y. Fang, R.J. Wang, G.H. Jiang, H. Jin, Y. Wang, X.K. Sun, S. Wang, T. Wang, *Bulletin of Materials Science* 35 (2012) 495–499.
- [34] A.R. Liu, S.M. Wang, Y.R. Zhao, Z. Zheng, *Materials Chemistry and Physics* 99 (2006) 131–134.
- [35] Y. Iizuka, T. Kubo, A. Nakahira, D. Onodera, N. Ozawa, T. Yao, *Applied Catalysis B: Environmental* 76 (2007) 51–56.
- [36] L.S. Wang, M.W. Xiao, X.J. Huang, Y.D. Wu, *Journal of Hazardous Materials* 161 (2009) 49–54.
- [37] A. Kundu, R.K. Layek, A. Kuila, A.K. Nandi, *ACS Applied Materials and Interfaces* 4 (2012) 5576–5582.
- [38] C.H. Fang, B.Y. Geng, J. Liu, F.M. Zhan, *Chemical Communications* 17 (2009) 2350–2352.
- [39] C.H. Wu, Y.Z. Zhang, S. Li, H.J. Zheng, H. Wang, J.B. Liu, K.W. Li, H. Yan, *Chemical Engineering Journal* 178 (2011) 468–474.
- [40] J. Lin, R.L. Zong, M. Zhou, Y.F. Zhu, *Applied Catalysis B: Environmental* 89 (2009) 425–431.
- [41] Y.J. Wang, R. Shi, J. Lin, Y.F. Zhu, *Applied Catalysis B: Environmental* 100 (2010) 179–183.
- [42] T.G. Xu, L.W. Zhang, H.Y. Cheng, Y.F. Zhu, *Applied Catalysis B: Environmental* 101 (2011) 382–387.